Control of heterogeneous, layered successions on shallow-level magma emplacement and host rock deformation

Craig Magee[1]*, Domenico Montanari[2], Giacomo Corti[2]

[1]Institute of Geophysics and Tectonics, School of Earth and Environment, University of Leeds, Leeds, LS2 9JT, UK

[2]Institute of Geosciences and Earth Resources, National Research Council of Italy (CNR), Via La Pira 4, 50121, Florence, Italy

*corresponding author: c.magee@leeds.ac.uk

Abstract

Host rock deformation in active volcanic settings can signal and be used to constrain magma emplacement. Yet it is difficult to evaluate the accuracy of intrusion parameters derived from inversion of deformation signals because we cannot test estimates by directly accessing the magma body. Physical modelling is thus critical to understanding how intrusion translates into host rock deformation, particularly surface uplift and/or subsidence, because we can use transparent materials or excavate models to view the actual intrusion geometry. However, few physical models have investigated how a heterogeneous, layered host material impacts magma emplacement, despite evidence suggesting the presence of weak layers can control intrusion style and geometry. We conduct several models that simulate emplacement of a felsic magma at ~6 km depth within a granular (sand) host rock; in two of our models we incorporate two, thin, weak microbead layers into the layered host material. We show that intrusion solely within the granular material is primarily accommodated by lateral contraction (compaction and folding) of the host material, resulting in a dyke-like intrusion that erupted. When the microbead layers were present, a cone sheet and saucer-shaped sill preferentially formed, without erupting, accommodated by forced folding. Furthermore, we demonstrate that surface deformation does not simply reflect the complexity of the intrusion geometry or internal host material deformation. Overall, our results indicate that physical models should further explore the role of host material heterogeneity on magma emplacement.

Keywords: Forced fold; Sill; Dyke; Physical model; Magma emplacement

Introduction

Sill emplacement in the shallow subsurface may be accommodated by roof uplift (e.g., Cruden, 1998; Hansen and Cartwright, 2006; Johnson and Pollard, 1973; Pollard and

Johnson, 1973). Such roof uplift, a form of forced folding (Stearns, 1978), can deform the free surface (e.g., Agirrezabala, 2015; Galland, 2012a; Magee et al., 2017a; Montanari et al., 2017; Trude et al., 2003; van Wyk de Vries et al., 2014). By identifying, monitoring, and inverting the surface expression of intrusion-induced forced folding at active volcanoes we can locate subsurface sills (and other intrusions) and constrain their geometry, size, and depth (e.g., Biggs et al., 2009; Castro et al., 2016; Pagli et al., 2012; Sturkell et al., 2006); this method has proved critical to volcanic hazard assessment (e.g., Ebmeier et al., 2018; Magee et al., 2018; Sparks et al., 2012). However, computational restrictions mean inversions of measured surface deformation typically assume magma body geometries are simple and deformation occurs via elastic or visco-elastic processes (e.g., Galland, 2012a; Magee et al., 2019a; Poppe et al., 2019). Yet field observations and 3D seismic reflection images of ancient intrusions and forced folds reveal they have complex geometries and inelastic space-making mechanisms can simultaneously accommodate magma (e.g., Galland et al., 2019; Morgan et al., 2008; Schmiedel et al., 2017; Schmiedel et al., 2019; Schofield et al., 2012; Spacapan et al., 2017). Key barriers to deciphering how intrusion translates into surface deformation and, thereby, improving hazard assessment are that it is difficult to: (i) assess how simplifying intrusion geometries and deformation processes influences inversion accuracy, because we cannot test predictions without direct access to active volcanic plumbing systems (Galland, 2012a); and (ii) unravel intrusion and forced fold dynamics from ancient examples where magmatism has long-since ceased (e.g., Magee et al., 2017a).

Physical modelling is a powerful tool in studying roof uplift above sills because we can quantify how intrusions, forced folds, and inelastic deformation structures evolve through time, thereby helping to bridge the gap between studies capturing short-lived emplacement events and those examining the final product of magmatism (e.g., Galland, 2012a; Guldstrand et al., 2017; Kavanagh et al., 2015; Kavanagh et al., 2018; Montanari et al., 2017; Poppe et al., 2019; Schmiedel et al., 2017; Schmiedel et al., 2019).

Here we present a series of physical models that test how heterogeneous, layered media impacts the geometry of intrusions and associated host rock deformation structures, particularly forced folds. The rationale for this study is that measured disparities between intrusion thickness and forced fold amplitude, of seismically imaged sill-fold pairs, suggest inelastic deformation within heterogeneous, layered host rock sequences can accommodate a significant proportion of the magma volume (Hansen and Cartwright, 2006; Jackson et al., 2013; Magee et al., 2013; Magee et al., 2017b). If similar interplays between elastic bending and inelastic deformation accommodate magma emplacement in active volcanic settings, inverting surface displacements using elastic models may thus introduce inaccuracies in retrieved intrusion parameters. However, most seismic-based studies do not account for burial-related compaction of forced folds, which decreases any disparities between measured fold amplitudes and intrusion thickness, implying elastic bending is the dominant space-making mechanism (Magee et al., 2019b). Whilst few physical modelling experiments have examined how layering of different host rock lithologies controls translation of magma emplacement to surface deformation (cf. Gressier et al., 2010), they can allow us to quantify sill-fold pairs in 3D without needing to account for compaction (e.g., Galland, 2012a; Guldstrand et al., 2017; Montanari et al., 2017). Our results show that, with all other parameters kept the same, introducing weak microbead layers with the granular host material changes the intrusion style from dyke-like to sill-like. Furthermore, our models demonstrate that complex intrusion geometries and the internal deformation patterns within a forced fold are not necessarily reflected by contemporaneous surface deformation.

Methods

The aim of our physical model experiment series is to examine how the presence of weak layers in a heterogeneous host rock succession impact accommodation of intruding magma, and how intrusion translates into surface deformation. Experiments were performed at the Tectonic Modeling Laboratory of the CNR-IGG and of the Department of Earth Sciences in Florence, Italy, and involved injecting a magma analogue into an overlying brittle overburden (Fig. 1A). The models were built within a Plexiglas box with internal dimensions of 33 × 38 × 13.5 cm. Magma was injected from a syringe via a cylindrical PVC pipe (4 mm in internal diameter; D_{inlet}), with the inlet point located within the analogue brittle overburden 10 mm from the basal interface (i.e. at Horizon A; Figs 1A and B). We used a stepper motor connected to a central unit to maintain a constant and controlled flow rate of the magma analogue throughout the 110 minute maximum duration of each experiment (Fig. 1A); with this system we applied a constant magma analogue injection velocity of 25 cm/hr (Table 1; see Montanari et al., 2017). Our model set-up meant the space required to accommodate the intruded magma analogue was created by roof uplift, without the need to impose any artificial discontinuity to drive the emplacement trajectories (e.g., Fig. 1C).

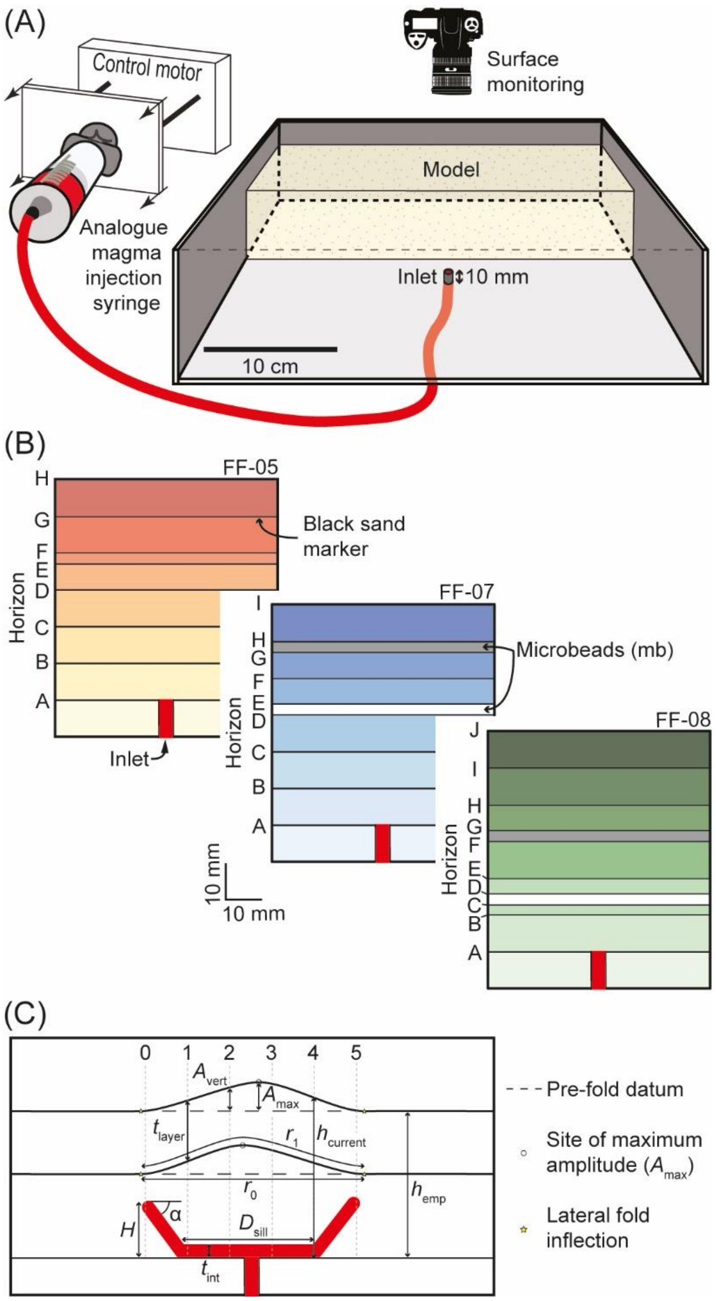

Figure 1: (A) Experimental apparatus sett-up; see text for details. (B) Host material configuration for models FF-5, FF-07, and FF-08. Microbead layers are depicted in FF-07 and FF-08 and are each 3 mm thick. (C) Schematic showing the different parameters measured, which include: current horizon height above injector ($h_{current}$); fold length (i.e. horizontal distance between fold inflections; r_0); fold line length (r_1); maximum amplitude (A_{max}); fold amplitude along selected vertical profiles (A_{vert}); layer thickness along selected

vertical profiles (t_{layer}); vertical intrusion thickness (t_{int}); intrusion transgressive height (H); inclined limb dip (α); inner sill diameter (D_{sill}); and magma emplacement depth (h_{emp}).

Table 1: Model characteristics for experiments FF-05, FF-07, and FF-08

Models	Injection velocity [cm/hr]	Time [minutes]	Injected volume [cm^3]	Model thickness [mm]	Host rock structure⁺
FF-05*	25	28	13	70	
FF-07	25	110	38.5	70	
FF-08	25	110	38.5	70	

*Stopped when erupted
⁺grey = sand, black = 3 mm thick microbead layers

Material properties

The brittle behaviour of the upper crustal rocks was simulated by layers composed of a mixture of quartz (70%) and K-feldspar (30%) sand with grain dimensions <250 μm, an angle of internal friction of 43°, cohesion of ~10 Pa, and a density of 1408 kg m^{-3} (Table 2; Montanari et al., 2017). Black quartz sand was sprinkled between each layer to provide marker horizons (Fig. 1B). Our control model, FF-05, comprises a homogeneous host rock consisting of seven distinct sand layers above the inlet (Fig. 1B). A heterogeneous overburden was replicated in two models (FF-07 and FF-08), by placing two layers of glass microbeads at different stratigraphic positions between sand layers (Fig. 1B); these microbead layers represent weaker frictional décollement horizons, relative to the sand layers, and simulate the presence of shales or marls interbedded with sandstone in nature. The microbeads have mean diameters of 200 μm, an angle of internal friction of 20–22°, cohesion of ~10 Pa, and a density of 1480 kg m^{-3} (Table 2). For a magma analogue we used pure vegetable polyglycerine-3 (PG3), a low-viscosity Newtonian fluid with a viscosity of 17 Pa s and density of ~1190 kg m^{-3} (Table 2; Montanari et al., 2017).

Table 2: Values of physical parameters in nature and experiments, and their experiment/nature ratio

Parameter		Models	Nature	Model/Nature ratio
Length (l) [m]		0.01	1000	10^{-5}
Brittle layer (sand mixture)	Density (ρ) [kg m^{-3}]	1408	~2700	~0.5
	Internal friction coefficient	1.1	0.85-1	1.3-1.1
	Cohesion (*C*), Pa	10	~10^{7}	1× 10^{-6}
Brittle dècollement (microbeads)	Density (ρ) [kg m^{-3}]	1480	~2600	0.57
	Internal friction coefficient	~0,40	0.25–0.52	~1
	Cohesion (*C*), Pa	10	4.4 10^{6}	2.2 10^{-6}
Magma PG3	Density (ρ) [kg m^{-3}]	1190	~2400	~0.5
	Viscosity (η) [Pa s]	17	~4 ×10^{12}	4.25 × 10^{-12}
Gravity (*g*) [m s^{-2}]		9.81	9.81	1
Stress (σ) [Pa]				~5 × 10^{-6}

Scaling

The models were scaled according to the principles of geometric, dynamic, and kinematic similarity (Hubbert, 1937; Ramberg, 1981). We used a length scaling ratio l^* (where * denotes the ratio between the model and natural values) of 10^{-5}, such that 10 mm in the models corresponds to 1 km in nature. The overburden above the top of the injection inlet, at the start of each model run was 60 mm (Fig. 1B), which thus corresponds to an initial emplacement depth of 6 km. Microbead layers added to models FF-07 and FF-08 were each 3 mm thick (Fig. 1B). Both models and nature have the same gravitational acceleration (g), imposing a scale factor of $g^*=1$. The density ratio (ρ^*) is ~0.5, resulting from the ratio between the analogue granular material (~1400 kg m^{-3}) and natural rocks (~2700 kg m^{-3}) (e.g., Schellart, 2000), as well as the ratio between our magma analogue (~1200 kg m^{-3}) and a natural granitic magma at emplacement conditions (~2400 kg m-3; e.g., Montanari et al., 2010). These ratios result in a stress scaling ratio ($\sigma^* = \rho^* g^* l^*$) of ~5 × 10^{-6}. The stress scaling ratio is related to the scaling ratios of strain rate (ε*), viscosity (η∗), and velocity of deformation (V*), by the relationship $\sigma* = \eta* \varepsilon* = \eta* (V*/l*)$. Our applied magma injection velocity in the models (2.5 cm/hr) thus scales to natural magma ascent rates of ~0.02 km/yr for viscosities of a natural felsic magma (i.e. ~4 $\times 10^{12}$; e.g., Merle, 2015).

Measurements

During the experiments, deformation was monitored through top-view photos taken at regular five-minute time intervals (Fig. 1A). At the end of each experiment, the models were watered, frozen, and cut with a saw to obtain cross-sections that could be used to analyse internal deformation (e.g., Fig. 1C). We note that in the presented cross-sections, a percolation aureole has developed around the intrusions, which occurs as polyglycerols leach out of the magma during wetting of the model (e.g., Galland et al., 2007; Galland et al., 2015; Montanari et al., 2017); these percolation aureoles do not impact the geometry of intrusion-induced deformation structures. Parameters measured for each model include: current horizon height above injector (h_{current}); fold length (i.e. horizontal distance between fold inflections; r_0); fold line length (r_1); maximum amplitude (A_{max}); fold amplitude along selected vertical profiles (A_{vert}); layer thickness along selected vertical profiles (t_{layer}); vertical intrusion thickness (t_{int}); intrusion transgressive height (H); inclined limb dip (α); inner sill diameter (D_{sill}); magma emplacement depth (h_{emp}), which is equal to the depth of the injector inlet beneath the model surface; and the diameter of the fold at the model surface (D_{fold}) (Fig. 1C). Fold measurements were collated from all deformed horizons. We also calculate the linear strain (ε_r) across the fold, which describes its change in length ($\Delta r = r_0 - r_1$) during deformation (Fig. 1C) whereby:

$$\varepsilon_r = \Delta r / r_0$$

Limitations and errors

Whilst our models are scaled to natural systems, the values derived to describe natural parameters are typically averages and/or assume specific magma or host rock compositions. Physical modelling of magma intrusions therefore involves several simplifications, primarily concerning the rheological properties of the analogue magma, the geometry of the magma feeder system, magma injection rates, cooling and crystallization of the magma, and variations in rheology and strength of the host rocks during emplacement (e.g., Galland, 2012b; Galland et al., 2006; Montanari et al., 2017). Adopting these simplifications limits the applicability of our models to examining natural systems. For example, our experiments simulate deformation induced by emplacement of felsic magma (Table 2), meaning our results cannot easily be compared to natural mafic systems and associated forced folds, which are the focus of most seismic reflection studies (e.g., see Magee et al., 2019b and references therein). In addition to adopting several simplifications, in this experimental series we could not quantify evolution of the model interior through time, since the host rock materials used are opaque and sectioning could only be conducted after the end of each model run (Kavanagh et al., 2018). Finally, we consider human error could introduce errors of up to ±5% to our measurements of intrusions and deformation structures within the models.

Results

In the homogeneous host rock model (FF-05), where all layers comprise sand, the intrusion has a dyke-like geometry with minor (<10 mm wide), sill- and laccolith-like asperities formed at most layer boundaries (except for Horizon G; Fig. 2A). Horizons A-F are subtly downwarped by <2 mm where intersected by the intrusion but small-to-moderate amplitude antiforms occur adjacent to the intrusion at horizons B-F; the intrusion-adjacent antiforms at horizons B-D occur on the right-hand side of the intrusion and have maximum amplitudes (A_{max}) of 0.6–0.7 mm, whilst those at horizons E and F occur on the left-hand side of the intrusion and have A_{max} values of 2.1 mm and 2.7 mm, respectively (Fig. 2A; Table. 3). Broad antiforms are developed at horizons G and H, which have A_{max} values of 3.9 mm and 2.3 mm, respectively (Fig. 2A; Table 3). The surface deformation associated with the Horizon H antiform reveals the fold is roughly circular, i.e. it is dome-shaped, with a diameter (D_{fold}) of ~40 mm. Eruption occurred at the outer fold inflection point and minor extensional faults and fractures, with variable orientations, are present across the fold crest (Fig. 2A).

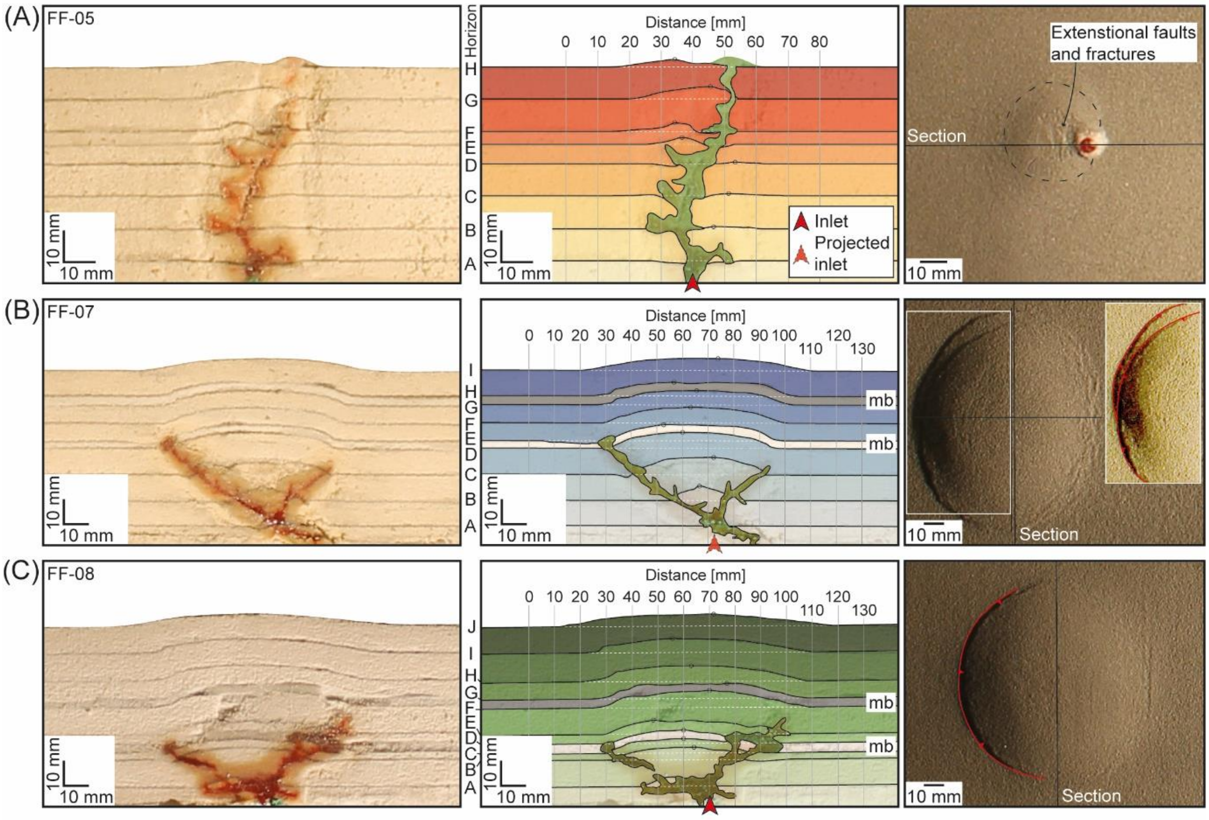

Figure 2: Uninterpreted and interpreted photographs of cross-sections through, as well as a plan-view of the final model geometry, for experiments FF-05 (A), FF-07 (B), and FF-08 (C). For each cross-section, a series of vertical profiles 10 mm apart were arbitrarily imposed and used to focus measurements (see Fig. 1C).

Table 3: Data describing maximum amplitude and linear strain across model horizons

Model	Horizon	Horizon height above inlet ($h_{current}$) [mm]	Maximum amplitude (A_{max}) [mm]	Intrusion thickness beneath A_{max} (t_{int}) [mm]	Fold length (r_0) [mm]	Fold line length (r_1) [mm]	Linear strain (ε_r)
	H	60	02.3	15.2	041.5	041.7	0.004
	G	50	03.9	13.0	035.2	036.9	0.049
	F	40	02.7	15.2	033.7	035.6	0.057
FF-05	E	36	02.1	23.2	027.4	028.2	0.029
	D	30	00.6	00.0	035.3	N/A*	N/A
	C	20	00.6	02.5	048.9	N/A	N/A
	B	10	00.7	01.6	018.3	N/A	N/A
	I	60	04.8	06.1	092.8	093.4	0.006
	H	50	05.5	02.6	082.4	085.7	0.039
	G	47	05.6	03.3	079.8	081.0	0.015
FF-07	F	40	06.2	01.5	074.3	075.8	0.020
	E	33	06.3	02.9	073.4	075.8	0.032
	D	30	06.3	01.5	070.3	071.9	0.023
	C	20	06.8	06.0	052.6	055.5	0.056
	B	10	05.7	04.5	027.8	030.7	0.107
	J	60	04.6	07.6	105.7	106.6	0.009
	I	50	05.4	03.7	088.8	089.5	0.008
	H	40	06.1	07.0	088.6	090.4	0.020
	G	33	05.9	06.1	084.1	087.2	0.038
FF-08	F	30	06.6	09.5	083.9	085.6	0.020
	E	20	05.6	04.4	072.6	075.2	0.035
	D	16	05.2	05.7	068.2	069.3	0.016
	C	12	05.6	05.7	066.2	068.2	0.030
	B	10	05.1	08.5	053.1	N/A	N/A

*N/A = could not be measured because intrusion obscured fold

Both models containing interbedded microbeads and sand layers (i.e. FF-07 and FF-08; Fig. 1B) display sill-like intrusion geometries, with minor apophyses that appear to intrude down to the base of the model from the inlet, and do not feed eruptions (Figs 2B and C). The intrusion in FF-07 comprises two inclined limbs, depicting a ~69 mm wide 'V-shaped' morphology, with the 30 mm high (*H*), left-hand limb transgressing up to and feeding a minor sill within the lowermost microbead layer (i.e. Layer D-E) at a dip (α) of ~30° (Fig. 2B); the transgressive right-hand limb (*H* = ~23 mm; α = ~40°) stalls immediately above Horizon C (Fig. 2B). Model FF-08 contains a ~76 mm wide, saucer-shaped sill comprising a flat, concordant inner sill at Horizon A, with a diameter (D_{sill}) of ~30 mm, which passes laterally into two inclined limbs (Fig. 2C). The transgressive left-hand inclined limb of FF-08 (H = ~11 mm; α = ~20°), in the section presented, is separated from the main sill and stalls within the lowermost microbead layer (i.e. Layer C-D), where it appears to form a minor sill in (Fig. 2C). The right-hand inclined limb of FF-08 extends up to Layer E-F (H = ~25 mm; α = ~40°) (Fig. 2C); where the right-hand limb intersects Layer C-D, it displays a complex morphology and appears to intrude along the microbeads (Fig. 2C). Where inclined limbs of both FF-07 and FF-08 intersect folded horizons, they do so at the outer fold inflection points (Figs 2B and C). Surface deformation in FF-07 is characterised by an elliptical forced fold, ~110 × 90 mm, bound on its left-hand side by two arcuate reverse faults (Fig. 2B). The forced fold in FF-08, at the surface, is sub-circular, has a D_{fold} of ~10 mm, and is bound on its left-hand side by a single arcuate reverse faults (Fig. 2C). Within the FF-07 and FF-08 forced folds, all horizons from Horizon B to the top of the fold display smooth, antiform structures in cross-section (Figs 2B and C); A_{max} values for FF-07 range from 4.8–6.8 mm, and for FF-08 range from 4.6–6.6 mm (Figs 2B and C; Table 3). In all models, the location of A_{max} varies between horizons and is rarely situated directly above the inlet (Fig. 2).

Quantitative analysis

For all models, there is a strong (R^2 ≥0.90), positive correlation between fold line length (r_1) and horizon height above the inlet ($h_{current}$) (Figs 2, 3, and 4A); the exception to this relationship are the folds developed along horizons C and D in model FF-05 (Fig. 4A), but these measurements include wide areas where the horizons are downwarped (Fig. 2A). In models FF-07 and FF-08 there is no obvious correlation between the height of microbead layers and where deviations from the gradient of the linear regression trendline occur (Fig.

4A). All three models also show a similar pattern in how A_{max} increases and then decreases with $h_{current}$ (Figs 3 and 4B). For FF-05 there is little change in A_{max} and $h_{current}$ between horizons B-D, but then A_{max} steadily increases up to Horizon G (3.9 mm) before decreasing at Horizon H (2.3 mm) (Fig. 4B; Table 4); we note extensional faulting across the crest of the FF-05 forced fold may have reduced A_{max} along Horizon H (Fig. 2A). The A_{max} values for FF-07 increase from 5.7 mm at Horizon B to 6.8 mm at Horizon C, and then gradually decrease to 4.8 mm at Horizon I (Figs 3A and 4B; Table 4). From an A_{max} of 5.1 mm at Horizon B, the greatest A_{max} of FF-08 is 6.6 mm at Horizon F, which decreases to 4.6 mm at Horizon J (Figs 3B and 4B; Table 4). The A_{max} of the two top microbead horizons in FF-08 (i.e. D and G) are suppressed relative to the general trend of the data (Fig. 4B; Table 4). We note A_{max} also broadly increases and then decreases with r_1 (Figs 3 and 4C).

Table 4: Horizon amplitude measured along imposed vertical profiles

Model	Distance [mm]	Horizon amplitude (A_{vert}) [mm]									Intrusion thickness [mm]
		B	C	D	E	F	G	H	I	J	
FF-07	0	-	-	-	-	-	-	-	-	N/A	-
	10	-	-	-	-	-	-	-	-	N/A	-
	20	-	-	-	-	-	-	-	00.2	N/A	-
	30	-	-	-	-	00.3	00.5	00.3	01.6	N/A	05.3
	40	-	-	04.0	04.0	03.6	03.3	03.9	03.3	N/A	03.4
	50	-	04.7	05.5	06.1	05.5	05.1	05.1	03.9	N/A	05.5
	60	03.2	06.5	06.3	06.3	06.0	05.4	05.2	04.4	N/A	01.5
	70	04.8	06.8	06.2	06.0	06.0	05.5	05.4	04.8	N/A	05.0
	80	-	05.6	05.1	05.6	05.3	04.9	05.2	04.6	N/A	02.8
	90	-	02.2	02.9	03.6	03.4	04.1	04.8	03.8	N/A	01.8
	100	-	-	-	-	00.2	00.6	01.2	02.3	N/A	-
	110	-	-	-	-	-	-	-	00.3	N/A	-
	120	-	-	-	-	-	-	-	-	N/A	-
	130	-	-	-	-	-	-	-	-	N/A	-
FF-08	0	-	-	-	-	-	-	-	-	-	-
	10	-	-	-	-	-	-	-	-	-	-
	20	-	-	-	-	-	-	-	-	01.1	-
	30	-	-	-	00.3	01.0	00.9	01.8	02.7	03.1	04.1
	40	02.6	04.0	03.0	04.0	04.2	04.3	04.8	03.9	03.9	03.9
	50	04.4	04.9	04.9	05.4	05.1	05.4	05.6	05.2	04.4	07.8
	60	04.8	05.6	05.1	05.3	06.2	05.7	06.1	05.4	04.4	05.7
	70	04.1	05.0	04.1	04.8	06.5	05.7	06.2	05.1	04.6	09.5
	80	-	-	-	04.1	05.8	05.6	05.5	04.9	03.5	12.8
	90	-	-	-	03.2	04.0	03.9	04.1	03.4	03.1	07.1

100	-	-	-	-	01.5	01.4	01.9	01.7	02.3	01.9
110	-	-	-	-	-	-	-	-	00.7	-
120	-	-	-	-	-	-	-	-	-	-
130	-	-	-	-	-	-	-	-	-	-

- denotes sites where no measurement was obtained (e.g., there is no folding or no intrusion)

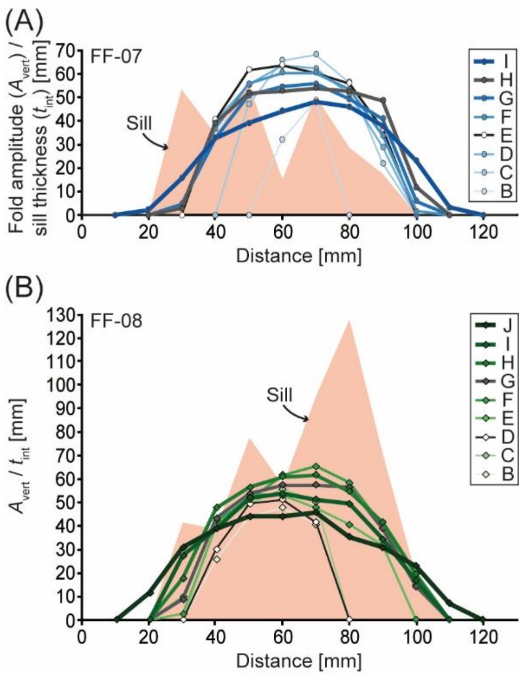

Figure 3: (A and B) Plots of fold amplitude, for each horizon, and sill thickness measured along the vertical profiles imposed on FF-07 and FF-08 (see Figs 2B and C; Table 4).

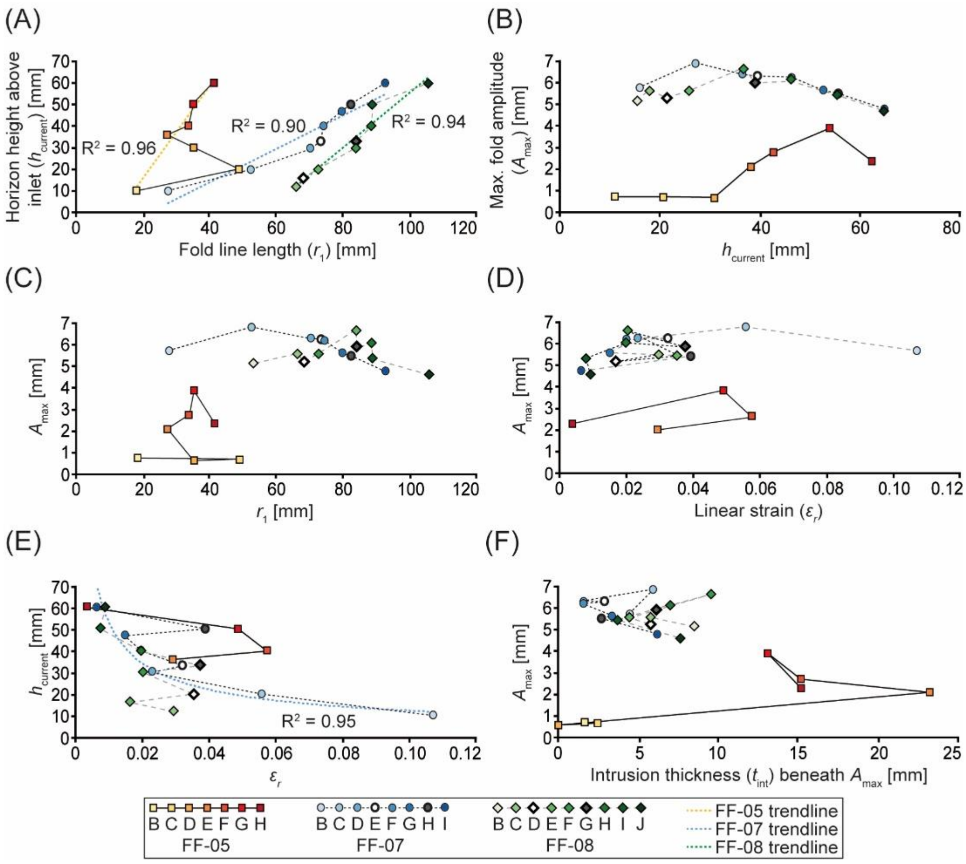

Figure 4: (A) Plot of fold line length and horizon height above inlet for FF-05, FF-07, and FF08. Linear regression trendlines also plotted. (B) Plot of horizon height above inlet and maximum fold amplitude for each horizon in the three models. (C) Plot of fold line length and maximum fold amplitude. (D) Plot of linear strain and maximum fold amplitude. (E) Plot of linear strain and horizon height above inlet. Power-law trendline shown for FF-07; trendline does not take into account the microbead layer values. (F) Plot of intrusion thickness measured along the imposed vertical profiles (Fig. 2) and the corresponding amplitude of folds along each horizon. For A-F, see Figure 1C and text for explanation of measured parameters.

There appears to be little, if no, correlation between the A_{max} of a given horizon and linear strain (ε_r) at the same structural level (Fig. 4D). However, there is a broad decrease in

ε_r, particularly for FF-07 and FF-08, from the lower horizons to the model top; important exceptions to this are the microbead layers that accommodate a disproportionate increase in ε_r (Fig. 4E). For example, horizons at the top of sand layers in FF-07 (i.e. horizons B, C, D, F, G, and I) describe a strong ($R^2 \geq 0.95$), power-law decay of ε_r with $h_{current}$ (Fig. 4E). Yet those horizons marking the top of microbead layers in FF-07 show higher ε_r values of 0.032 (Horizon E) and 0.039 (Horizon H) than the power-law trendline predicts (i.e. ~0.020 for Horizon E and ~0.012 for Horizon H; Fig. 4E). We note that whilst most horizons within models FF-07 and FF-08 have a smooth, bell-shaped profile in cross-section, the uppermost microbead layers (i.e. horizons H and G, respectively) have relatively flat-topped geometries (Fig. 3).

There appears to be little, if no, correlation between the A_{max} of a given horizon and the t_{int} of the underlying intrusion segment, particularly for models FF-07 and FF-08 (Fig. 4F). Whilst intrusion thickness does not seem to control amplitude magnitude (Fig. 4F), relative changes in t_{int} along-strike moderately ($R^2 = 0.46$ and 0.69 for FF-07 and FF-08, respectively) and positively correlate too and are broadly reflected in amplitude variations (Figs 3 and 5A). There is also a strong ($R^2 = 0.89$ and 0.95 for FF-07 and FF-08, respectively), positive correlation between A_{vert} across the top of the fold and the corresponding intrusion depth beneath A_{vert} (Figs 3 and 5B).

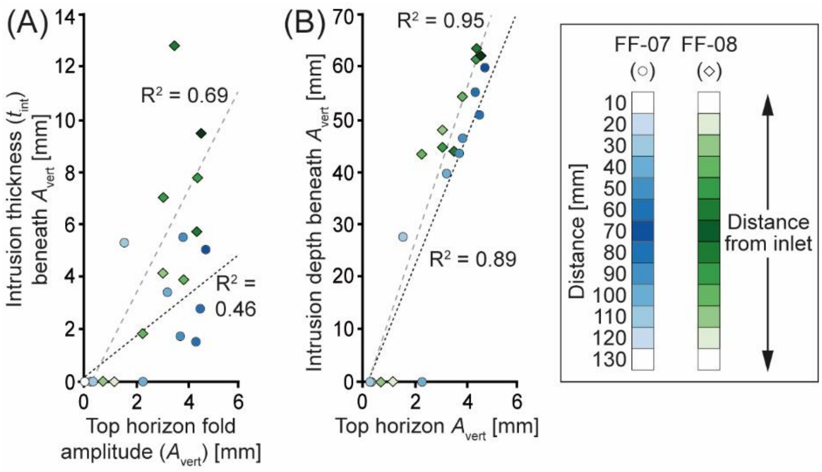

Figure 5: Plots of intrusion thickness (A) and depth (B) measured along the imposed vertical profiles against the corresponding amplitude of the top horizon (i.e. model surface) for models FF-07 and FF-08. Linear regression trendlines shown.

Layer thickness (t_{layer}) across the modelled forced folds is variable (Fig. 6; Table 5). Prominent apparent changes in t_{layer}, particularly relative reductions in thickness, are associated with where intrusions intersect a measured vertical profile (Figs 2 and 6). Model FF-05 displays the most prominent t_{layer} variations, with some layers showing localised thinning of up to ~5.2 mm (Layer F-G; Figs 6A and B). In all models, the top stratal layer thins across the fold crest and has thickened in the area encompassing the outer fold inflection points of its upper and lower bounding surfaces (Fig. 6). For example, in model FF-07, Layer H-I thickens by ~0.8 mm and ~1.2 mm across the outer edges of the forced fold, but thins by up to ~1.3 mm across its crest (Figs 6C and D; Table 5). Other layers in the three models, particularly those situated towards the top of their respective forced folds and the two microbead layers in model FF-07 (i.e. layers D-E and G-H), show similar thickness trends to the top layers (Fig. 6). In model FF-08, the microbead layers (i.e. layers C-D and F-G) primarily display evidence of thinning across the forced fold, by up to ~1.2 mm and ~1.8

mm, respectively; layers B-C, E-F, and G-H broadly thicken across the fold by up to ~1.4 mm, ~1.7 mm, and ~0.9 mm, respectively (Figs 6E and F).

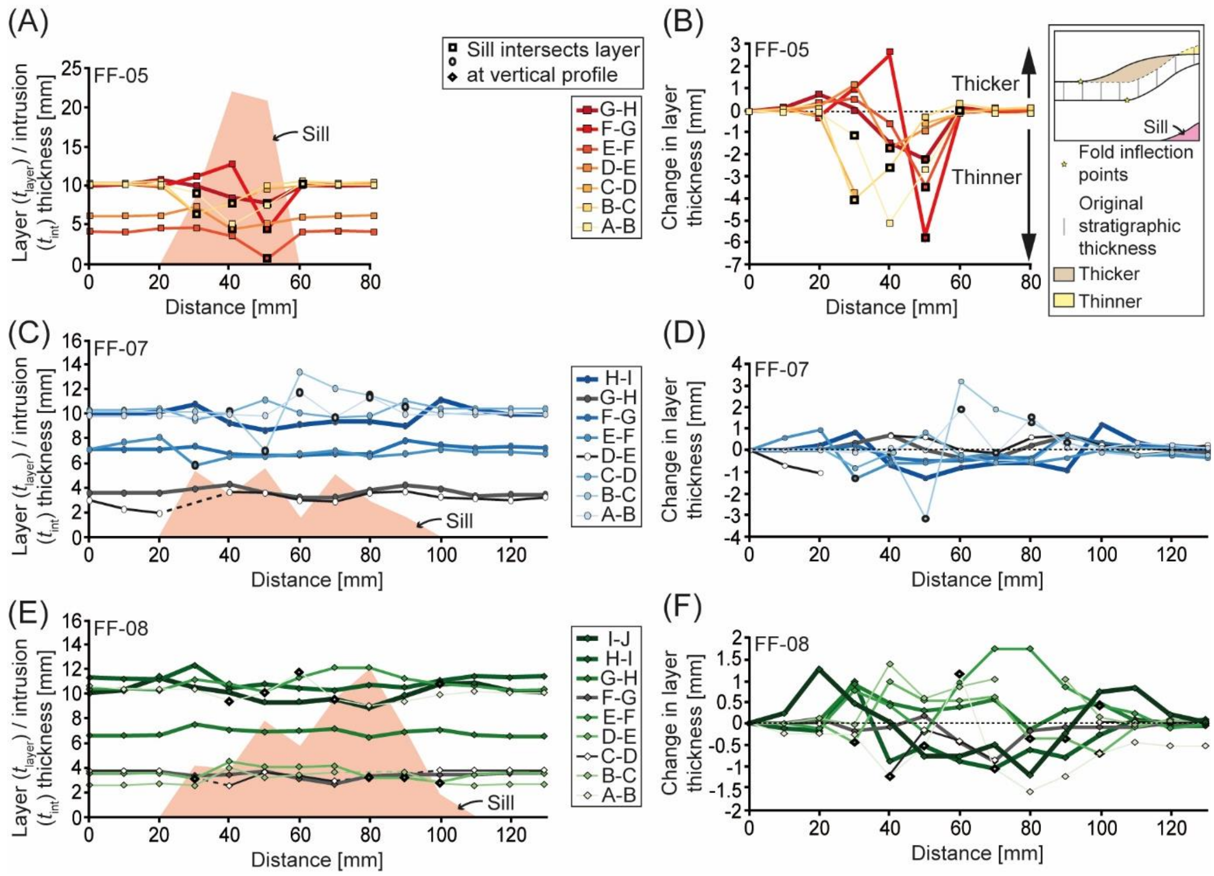

Figure 6: Plots examining layer thickness in models FF-05, FF-07, and FF-08. (A, C, and E) Plots of layer thickness, for each layer, and sill thickness measured along the vertical profiles imposed on the cross-sections. (B, D, and F) Change in layer thickness over the duration of the models. Inset in (B): schematic diagram showing how upwards broadening of a forced fold produces areas across the fold crest where layers are thinned, and zones of thickening over the fold inflections.

Table 5: Layer thickness measurements across the models where vertical profiles intersect

Model	Distance [mm]	Layer thickness (t_{layer}) [mm]								
		A-B	B-C	C-D	D-E	E-F	F-G	G-H	H-I	I-J
FF-05	0	10.2	10.3	10.1	06.1	04.1	10.2	10.0	N/A	N/A
	10	10.1	10.3	10.1	06.1	04.0	10.2	10.1	N/A	N/A

	20	10.1	10.5	09.9	06.1	04.5	09.9	10.8	N/A	N/A
	30	09.1	06.4	06.4	07.3	04.6	11.2	10.0	N/A	N/A
	40	*05.0**	*07.8*	-	*04.4*	03.5	12.8	08.5	N/A	N/A
	50	07.5	10.0	09.5	05.1	*00.6*	*04.4*	07.8	N/A	N/A
	60	10.3	10.6	10.0	05.9	04.1	10.1	10.1	N/A	N/A
	70	10.1	10.3	10.1	06.1	04.1	10.2	10.0	N/A	N/A
	80	10.1	10.4	10.1	06.2	04.1	10.1	10.1	N/A	N/A
	0	09.8	10.1	10.2	02.9	07.1	07.1	03.5	09.9	N/A
	10	09.8	10.1	10.2	02.2	07.6	07.1	03.5	09.9	N/A
	20	09.8	10.1	10.4	01.9	08.0	07.1	03.5	10.1	N/A
	30	09.6	10.1	09.4	-	*05.8*	07.3	03.9	10.7	N/A
	40	09.9	*10.0*	*10.1*	03.6	06.5	06.7	04.2	09.2	N/A
	50	*09.8*	*06.9*	11.1	03.5	06.5	06.6	03.5	08.6	N/A
FF-07	60	*11.6*	13.3	10.0	02.9	06.7	06.6	03.2	09.1	N/A
	70	*09.6*	12.0	09.6	02.8	06.9	06.7	03.2	09.3	N/A
	80	*11.3*	*11.4*	09.8	03.5	06.5	06.7	03.8	09.3	N/A
	90	09.9	*10.5*	10.9	03.7	06.7	07.8	04.2	08.9	N/A
	100	09.9	10.0	10.4	03.2	07.1	07.4	03.9	11.1	N/A
	110	10.1	09.9	10.4	03.1	06.8	07.2	03.3	10.2	N/A
	120	10.0	10.0	10.4	02.9	06.8	07.3	03.4	09.9	N/A
	130	09.9	09.9	10.4	03.2	06.7	07.2	03.4	09.9	N/A
	0	10.6	02.6	03.8	03.5	10.3	03.5	06.6	11.3	10.1
	10	10.3	02.6	03.8	03.5	10.3	03.5	06.6	11.2	10.3
	20	10.3	02.7	03.8	03.5	10.2	03.6	06.6	11.1	11.4
	30	10.3	02.6	-	*03.1*	11.1	03.4	07.5	12.3	10.6
	40	*09.3*	04.0	02.6	04.5	10.8	03.4	07.1	10.4	10.1
	50	*10.1*	03.2	03.6	04.1	10.1	03.7	06.9	10.8	09.3
FF-08	60	*11.7*	03.4	03.4	04.1	11.3	03.1	07.0	10.4	09.3
	70	*09.5*	03.6	02.9	04.1	12.1	02.6	07.1	10.2	09.6
	80	*09.0*	-	-	03.2	12.1	03.4	06.4	10.7	08.9
	90	09.3	*03.6*	-	*03.2*	11.2	03.4	06.9	10.5	09.9
	100	09.9	02.7	03.8	*02.8*	10.8	03.4	07.1	11.0	10.8
	110	10.1	02.6	03.8	*03.4*	10.6	03.4	06.6	11.4	10.9
	120	10.1	02.6	03.8	03.6	10.2	03.5	06.5	11.3	10.3
	130	10.1	02.6	03.8	03.5	10.3	03.5	06.5	11.4	10.1

*measurements in italics correspond to where intrusion partly hinders thickness measurement
- denotes where intrusion completely obscures layer thickness

Discussion

The geometrical properties of intrusion-induced forced folds, produced purely by elastic bending of the overburden, are expected to mimic the shape and size of the magma body they accommodated (e.g., Galland, 2012a; Schmiedel et al., 2017). If elastic bending fully accommodates emplacement, we can therefore use the amplitude (and volume) of forced folds measured either at Earth's surface or in seismic reflection data as a proxy for intrusion thickness (and volume) (e.g., Hansen and Cartwright, 2006; Jackson et al., 2013). Yet our models show that: (i) the relatively smooth, dome-shaped folds do not capture the morphological complexity of the intrusions (Fig. 2): (ii) fold length (diameter) increases with height above the intrusion feeding site (Figs 3 and 4A); (iii) fold amplitude is locally variable but broadly decreases with height (Figs 3 and 4B), and is thus decoupled from intrusion thickness (Fig. 4F); and (iv) the weak microbead layers preferentially accommodate more linear strain (extension), and their layer thickness varies across the folds (Figs 4E and 6). These observations indicate the intruded magma volume was not purely accommodated by elastic bending, supporting an array of previous physical modelling studies that have shown the translation of magma emplacement into surface deformation is complex (e.g., Galland, 2012a; Galland et al., 2019; Poppe et al., 2019; Schmiedel et al., 2019). Here, we discuss how our results contribute to our understanding of specific relationships between magma emplacement style, host rock behaviour during deformation, and intrusion geometry.

Intrusion style and host rock lithology

Numerous physical modelling experiments have examined how host rock properties (e.g., rock strength, and cohesion) impact intrusion morphology (e.g., Abdelmalak et al., 2012; Galland, 2012a; Galland et al., 2014; Guldstrand et al., 2017; Kavanagh et al., 2018; Kavanagh et al., 2006; Kervyn et al., 2009; Mathieu et al., 2008; Montanari et al., 2017; Poppe et al., 2019; Schmiedel et al., 2017; Schmiedel et al., 2019). For example, several experimental series injection of a magma analogue into a homogeneous and granular media have suggested massive intrusions (e.g. cryptodomes) typically form within low-strength material (i.e. low cohesion and angles of internal friction), whilst sheet intrusions (e.g. dyke, sills, and cone sheets) develop in material with moderate-to-high strengths (e.g., Poppe et al., 2019; Schmiedel et al., 2017; Schmiedel et al., 2019). However, variations between materials used and model set-ups mean comparing different experimental results, and nature, can be difficult (Poppe et al., 2019).

Galland et al. (2014) derived a series of dimensionless numbers to facilitate comparison between different experimental set-ups and nature. These dimensional parameters include the depth-to-size of the magma source (Π_1) and the dynamic ratio of viscous stresses due to magma flow and strength of the host rock (Π_2):

$$\Pi_1 = h_{\mathrm{emp}}/D_{\mathrm{inlet}}$$

where h_{emp} is the depth of the injector inlet and D_{inlet} is its inlet diameter (these correspond to *h* and *d*, respectively, in Galland et al., 2014).

$$\Pi_2 = (\eta v)/(C D_{\mathrm{inlet}})$$

where η is the analogue magma viscosity, v is the injection velocity, and C is the cohesion of the host material. Different intrusion morphologies, both observed in nature and created in experiments, can be distinguished on a plot of Π_1 vs Π_2 (Fig. 7) (Galland et al., 2014). Importantly, the Π_1 and Π_2 values for our three models are the same (i.e. 15 and 0.03, respectively), yet different intrusion geometries are produced depending on whether the host succession is homogeneous or heterogeneous (Figs 2 and 7).

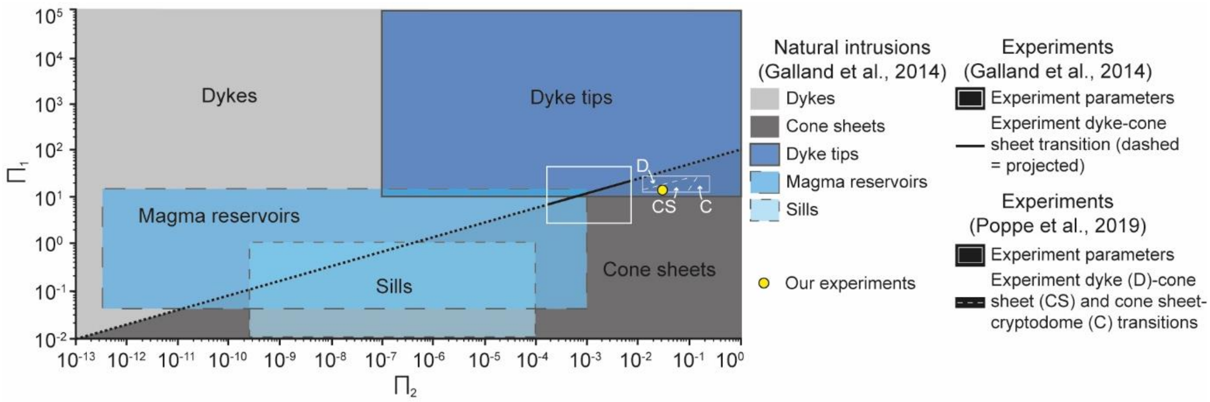

Figure 7: Plot of Π_1 versus Π_2, highlighting the approximate parameter space occupied by different natural intrusions and experiments, including our models (modified from Galland et al., 2014; Poppe et al., 2019).

It is clear from the model cross-sections that the magma analogue in FF-07 and FF-08 forms inclined sheets or a sill, respectively, immediately after exiting the inlet; in contrast, magma in FF-05 intrudes straight upwards (Fig. 2). Because we keep all other input parameters consistent (including Π_1 and Π_2), it seems likely that the presence of microbead layers has caused the intrusion geometry to change from being dyke-like in the homogeneous sand model (FF-05), to having a cone sheet (FF-07) or saucer-shaped sill (FF-08) appearance (Fig. 2). This change in the behaviour of the magma analogue upon exiting the inlet may imply the presence of the microbead layers influences emplacement style before there is any physical interaction between the two materials. The dyke-like intrusion geometry and adjacent downwarping of horizons A-E, flanked by zones of uplift, in model FF-05 imply space for the magma analogue was primarily generated by lateral contraction (compaction and folding) of the host material (Figs 2A and 8A); this is also consistent with thinning of layers A-B to D-E (Figs 5A and B). When the dyke-like intrusion reached Layer D-E and formed a small sill, it appears the reduced overburden meant space could be accommodated by the formation of broader, dome-shaped forced folds (Figs 2A and 8B). In contrast, we suggest the injection of the magma analogue in models FF-07 and FF-08 caused the microbeads layers to immediately ‘flow’ laterally as porosity reduced, producing a central low in layer thickness, allowing underlying sand layers directly above the inlet to bend upwards (Fig. 8C and D). The capability of the microbead layers to compress laterally is evidenced by: (i) injection of intrusion portions along the microbead layers, without producing adjacent increases in the layer thickness (Figs 2B, C, and 5C-F); and (ii) the irregular surfaces bounding the microbead layers and particularly their upper boundaries, which accommodate more strain than horizons between sand-sand layers (Fig. 4E). Furthermore, the frictional resistance between the microbead layers and adjacent sand layers would likely have been less than between sand-sand layers in FF-05, possibly meaning flexural sliding and thus folding was easier in FF-07 and FF-08 (Hansen and Cartwright, 2006; Pollard and Johnson, 1973).

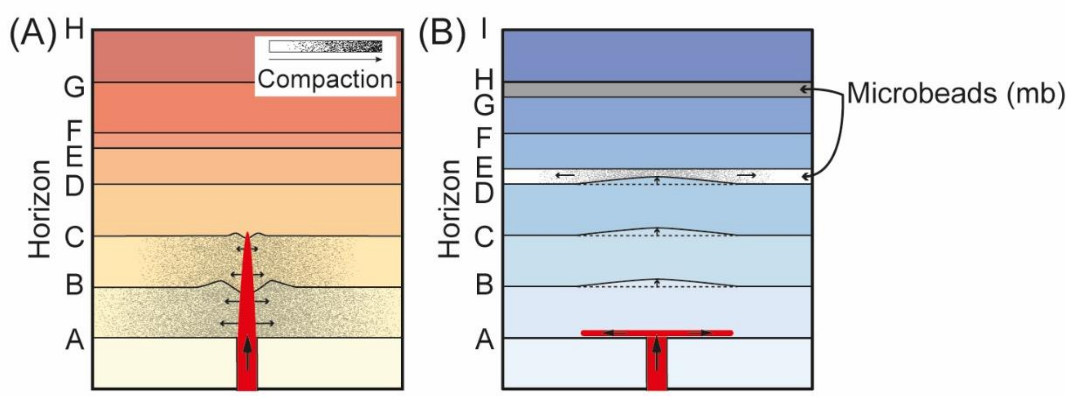

Figure 8: (A) Schematic showing how lateral contraction, by compaction and folding, of the lowermost sand layers in FF-05 accommodation dyke intrusion. (B) Diagram describing how compaction and lateral flow of microbead layers could accommodate uplift of the underlying sand, favouring development of a sill above the inlet.

Saucer-shaped sill emplacement

Saucer-shaped sills are commonly observed in sedimentary basins (e.g., Magee et al., 2016; Planke et al., 2005; Polteau et al., 2008; Pongwapee et al., 2019; Thomson and Hutton, 2004). It is broadly considered that the inclined limbs encompassing saucer-shaped sills develop in response to roof flexure and/or stress field rotation when once the inner sill diameter (D; here we use D_{sill}) is wide enough relative to its emplacement depth (d; here we use h_{emp}) (e.g., Fialko et al., 2001; Goulty and Schofield, 2008; Hansen and Cartwright, 2006; Jackson et al., 2013; Malthe-Sørenssen et al., 2004; Mathieu et al., 2008; Pollard and Holzhausen, 1979; Polteau et al., 2008). The ratio of $D_{\text{sill}}/h_{\text{emp}}$ required to promote intrusion of inclined limbs is ~3–5, assuming host rock deformation is purely elastic (Koch et al., 1981; Malthe-Sørenssen et al., 2004; Pollard and Holzhausen, 1979); Mathieu et al. (2008) reported inelastic host rock deformation allowed cup-shaped intrusions, which saucer-shaped sills are an example, to form when the $D_{\text{sill}}/h_{\text{emp}}$ ratio was only ~0.5. Assuming our cross-section through model FF-08 accurately captures the geometry of its intrusion, we calculate the inclined limbs formed when the $D_{\text{sill}}/h_{\text{emp}}$ ratio between the inner sill diameter (~30 mm) and emplacement depth (~60 mm) was ~0.5. Although a $D_{\text{sill}}/h_{\text{emp}}$ value of 0.5 is less than many studies predict, our result is consistent with those ratios recorded by Mathieu et al. (2008) and may similarly be potentially explained by the accommodation of magma by elastic *and* inelastic deformation.

Forced fold development

Our study supports recent physical model experiments by demonstrating dome-shaped forced folds can form, and be expressed at the free surface, above both dyke- and sill-like sheet intrusions (Fig. 2) (e.g., Galland, 2012a; Guldstrand et al., 2017; Poppe et al., 2019; Schmiedel et al., 2017). We also show the forced folds developed above the cone sheets and saucer-shaped sills widen and decrease in amplitude upwards (Figs 2B, C, and 3), consistent with previous suggestions that contemporaneous compaction of the overburden can partly accommodate strain (e.g., Hansen and Cartwright, 2006; Jackson et al., 2013; Morgan et al., 2008; Pollard and Johnson, 1973; Withjack et al., 1990); i.e. inelastic deformation suppresses the translation of magma emplacement into surface deformation.

Conclusion

Physical modelling has played a pivotal role in isolating and testing how different processes and material properties impact the style of magma emplacement. Yet few physical experiments involve a heterogeneous, layered host succession, despite field evidence and numerical modelling indicating the juxtaposition of different lithologies can control intrusion geometry and emplacement. Here, we present physical models that comprise a granular sand host interbedded with thin, weak layer of microbeads at least 13 mm above the magma analogue inlet; all model except the host succession configuration were kept constant. In our control experiment (no microbeads), the intrusion attained a dyke-like geometry before erupting, showing evidence of the magma analogue being accommodated by lateral contraction of the host material near its base and roof uplift (forced folding) near the surface. Where two layers of microbeads were incorporated into our models, the injected magma analogue forms either a cone sheet or saucer-shaped sill, accommodated primarily by forced folding, and did not erupt. We suggest that upon injection of the magma analogue, the microbead layers immediately began to compact and thin, accommodating uplift of the underlying sand layers and promoting sill intrusion; i.e. microbead layer compaction could occur before lateral contraction of the sand layer above the inlet. Our results support previous observations that the configuration of a layered host rock succession comprising lithologies with different mechanical properties can influence magma emplacement and intrusion geometry. Furthermore, we show that simple doming at the surface poorly reflects the internal structure of the forced folds or the complex geometry of underlying intrusions. Our models thus imply that the translation of magma emplacement into surface deformation is perhaps more complex than previously thought, questioning the accuracy of ground deformation inversions to recover to intrusion geometries, volumes, and location. Overall, physical modelling has a key role to play in developing our understanding of sub-volcanic magma emplacement and coupled surface deformation, but future experimental series should further explore the importance of heterogeneous host successions of these systems.

Acknowledgements

We are grateful for the Royal Society International Exchange grant (IE160574) that facilitated this collaboration; CM thanks Imperial College London who supported this grant.

References

1. Abdelmalak, M.M., Mourgues, R., Galland, O. and Bureau, D., 2012. Fracture mode analysis and related surface deformation during dyke intrusion: Results from 2D experimental modelling. Earth and Planetary Science Letters, 359: 93-105.
2. Agirrezabala, L.M., 2015. Syndepositional forced folding and related fluid plumbing above a magmatic laccolith: Insights from outcrop (Lower Cretaceous, Basque-Cantabrian Basin, western Pyrenees). Geological Society of America Bulletin: B31192. 31191.
3. Biggs, J., Anthony, E. and Ebinger, C., 2009. Multiple inflation and deflation events at Kenyan volcanoes, East African Rift. Geology, 37(11): 979-982.
4. Castro, J.M., Cordonnier, B., Schipper, C.I., Tuffen, H., Baumann, T.S. and Feisel, Y., 2016. Rapid laccolith intrusion driven by explosive volcanic eruption. Nature Communications, 7: 13585.
5. Cruden, A.R., 1998. On the emplacement of tabular granites. Journal of the Geological Society of London, 155(5): 853-862.

6. Ebmeier, S., Andrews, B., Araya, M., Arnold, D., Biggs, J., Cooper, C., Cottrell, E., Furtney, M., Hickey, J. and Jay, J.J.J.o.A.V., 2018. Synthesis of global satellite observations of magmatic and volcanic deformation: implications for volcano monitoring & the lateral extent of magmatic domains. 7(1): 2.

7. Fialko, Y., Khazan, Y. and Simons, M., 2001. Deformation due to a pressurized horizontal circular crack in an elastic half-space, with applications to volcano geodesy. Geophysical Journal International, 146(1): 181-190.

8. Galland, O., 2012a. Experimental modelling of ground deformation associated with shallow magma intrusions. Earth and Planetary Science Letters, 317: 145-156.

9. Galland, O., 2012b. Experimental modelling of ground deformation associated with shallow magma intrusions. Earth and Planetary Science Letters, 317-318: 145-156.

10. Galland, O., Burchardt, S., Hallot, E., Mourgues, R. and Bulois, C., 2014. Dynamics of dikes versus cone sheets in volcanic systems. Journal of Geophysical Research: Solid Earth, 119(8): 6178-6192.

11. Galland, O., Cobbold, P.R., de Bremond d'Ars, J. and Hallot, E., 2007. Rise and emplacement of magma during horizontal shortening of the brittle crust: Insights from experimental modeling. Journal of Geophysical Research: Solid Earth (1978–2012), 112(B6).

12. Galland, O., Cobbold, P.R., Hallot, E., de Bremond d'Ars, J. and Delavaud, G., 2006. Use of vegetable oil and silica powder for scale modelling of magmatic intrusion in a deforming brittle crust. Earth and Planetary Science Letters, 243(3–4): 786-804.

13. Galland, O., Holohan, E., de Vries, B.v.W. and Burchardt, S., 2015. Laboratory modelling of volcano plumbing systems: a review, Physical Geology of Shallow Magmatic Systems. Springer, pp. 147-214.

14. Galland, O., Spacapan, J.B., Rabbel, O., Mair, K., Soto, F.G., Eiken, T., Schiuma, M. and Leanza, H.A.J.J.o.S.G., 2019. Structure, emplacement mechanism and magma-flow significance of igneous fingers–Implications for sill emplacement in sedimentary basins. 124: 120-135.

15. Goulty, N.R. and Schofield, N., 2008. Implications of simple flexure theory for the formation of saucer-shaped sills. Journal of Structural Geology, 30(7): 812-817.

16. Gressier, J.-B., Mourgues, R., Bodet, L., Matthieu, J.-Y., Galland, O. and Cobbold, P., 2010. Control of pore fluid pressure on depth of emplacement of magmatic sills: An experimental approach. Tectonophysics, 489(1): 1-13.

17. Guldstrand, F., Burchardt, S., Hallot, E. and Galland, O., 2017. Dynamics of surface deformation induced by dikes and cone sheets in a cohesive Coulomb brittle crust. Journal of Geophysical Research: Solid Earth, 122(10): 8511-8524.

18. Hansen, D.M. and Cartwright, J., 2006. The three-dimensional geometry and growth of forced folds above saucer-shaped igneous sills. Journal of Structural Geology, 28(8): 1520-1535.

19. Hubbert, M.K., 1937. Theory of scale models as applied to the study of geologic structures. Geological Society of America Bulletin, 48(10): 1459-1520.

20. Jackson, C.A.-L., Schofield, N. and Golenkov, B., 2013. Geometry and controls on the development of igneous sill–related forced folds: A 2-D seismic reflection case study from offshore southern Australia. Geological Society of America Bulletin, 125(11-12): 1874-1890.

21. Johnson, A.M. and Pollard, D.D., 1973. Mechanics of growth of some laccolithic intrusions in the Henry mountains, Utah, I: field observations, Gilbert's model, physical properties and flow of the magma. Tectonophysics, 18(3): 261-309.

22. Kavanagh, J., Boutelier, D. and Cruden, A., 2015. The mechanics of sill inception, propagation and growth: Experimental evidence for rapid reduction in magmatic overpressure. Earth and Planetary Science Letters, 421: 117-128.

23. Kavanagh, J.L., Engwell, S.L. and Martin, S.A., 2018. A review of laboratory and numerical modelling in volcanology. Solid Earth, 9(2): 531-571.

24. Kavanagh, J.L., Menand, T. and Sparks, R.S.J., 2006. An experimental investigation of sill formation and propagation in layered elastic media. Earth and Planetary Science Letters, 245(3-4): 799-813.

25. Kervyn, M., Ernst, G.G.J., van Wyk de Vries, B., Mathieu, L. and Jacobs, P., 2009. Volcano load control on dyke propagation and vent distribution: Insights from analogue modeling. Journal of Geophysical Research: Solid Earth, 114(B3): B03401.

26. Koch, F., Johnson, A. and Pollard, D., 1981. Monoclinal bending of strata over laccolithic intrusions. Tectonophysics, 74(3): T21-T31.

27. Magee, C., Bastow, I.D., de Vries, B.v.W., Jackson, C.A.-L., Hetherington, R., Hagos, M. and Hoggett, M., 2017a. Structure and dynamics of surface uplift induced by incremental sill emplacement. Geology, 45(5): 431-434.

28. Magee, C., Briggs, F. and Jackson, C.A.-L., 2013. Lithological controls on igneous intrusion-induced ground deformation. Journal of the Geological Society, 170(6): 853-856.

29. Magee, C., Ernst, R.E., Muirhead, J., Phillips, T. and Jackson, C.A.-L., 2019a. Magma Transport Pathways in Large Igneous Provinces: Lessons from Combining Field Observations and Seismic Reflection Data. In: R. Srivastava, R. Ernst and P. Peng (Editors), Dyke Swarms of the World: A Modern Perspective. Springer, pp. 45-85.

30. Magee, C., Hoggett, M., Jackson, C.A.-L. and Jones, S.M., 2019b. Burial-Related Compaction Modifies Intrusion-Induced Forced Folds: Implications for Reconciling Roof Uplift Mechanisms Using Seismic Reflection Data. 7(37).
31. Magee, C., Jackson, C.A.-L., Hardman, J.P. and Reeve, M.T., 2017b. Decoding sill emplacement and forced fold growth in the Exmouth Sub-basin, offshore northwest Australia: Implications for hydrocarbon exploration. Interpretation, 5(3): SK11-SK22.
32. Magee, C., Muirhead, J.D., Karvelas, A., Holford, S.P., Jackson, C.A., Bastow, I.D., Schofield, N., Stevenson, C.T., McLean, C. and McCarthy, W., 2016. Lateral magma flow in mafic sill complexes. Geosphere: GES01256. 01251.
33. Magee, C., Stevenson, C.T., Ebmeier, S.K., Keir, D., Hammond, J.O., Gottsmann, J.H., Whaler, K.A., Schofield, N., Jackson, C.A. and Petronis, M.S.J.J.o.P., 2018. Magma plumbing systems: a geophysical perspective. 59(6): 1217-1251.
34. Malthe-Sørenssen, A., Planke, S., Svensen, H. and Jamtveit, B., 2004. Formation of saucer-shaped sills. In: C. Breitkreuz and N. Petford (Editors), Physical geology of high-level magmatic systems. Geological Society, London, Special Publications, pp. 215-227.
35. Mathieu, L., van Wyk de Vries, B., Holohan, E.P. and Troll, V.R., 2008. Dykes, cups, saucers and sills: Analogue experiments on magma intrusion into brittle rocks. Earth and Planetary Science Letters, 271(1–4): 1-13.
36. Merle, O., 2015. The scaling of experiments on volcanic systems. Frontiers in Earth Science, 3(26).
37. Montanari, D., Bonini, M., Corti, G., Agostini, A., Del Ventisette, C., 2017. Forced folding above shallow magma intrusions: Insights on supercritical fluid flow from analogue modelling. Journal of Volcanology and Geothermal Research, 345: 67-80.

38. Montanari, D., Corti, G., Sani, F., Del Ventisette, C., Bonini, M. and Moratti, G., 2010. Experimental investigation on granite emplacement during shortening. Tectonophysics, 484(1-4): 147-155.

39. Morgan, S., Stanik, A., Horsman, E., Tikoff, B., de Saint Blanquat, M. and Habert, G., 2008. Emplacement of multiple magma sheets and wall rock deformation: Trachyte Mesa intrusion, Henry Mountains, Utah. Journal of Structural Geology, 30(4): 491-512.

40. Pagli, C., Wright, T.J., Ebinger, C.J., Yun, S.-H., Cann, J.R., Barnie, T. and Ayele, A., 2012. Shallow axial magma chamber at the slow-spreading Erta Ale Ridge. Nature Geoscience, 5(4): 284-288.

41. Planke, S., Rasmussen, T., Rey, S.S. and Myklebust, R., 2005. Seismic characteristics and distribution of volcanic intrusions and hydrothermal vent complexes in the Vøring and Møre basins. In: A.G. Doré (Editor), Petroleum Geology: North-West Europe and Global Perspectives - Proceedings of the 6th Petroleum Geology Conference. Geological Society, London, pp. 833-844.

42. Pollard, D.D. and Holzhausen, G., 1979. On the mechanical interaction between a fluid-filled fracture and the Earth's surface. Tectonophysics, 53(1-2): 27-57.

43. Pollard, D.D. and Johnson, A.M., 1973. Mechanics of growth of some laccolithic intrusions in the Henry Mountains, Utah, II: bending and failure of overburden layers and sill formation. Tectonophysics, 18(3): 311-354.

44. Polteau, S., Mazzini, A., Galland, O., Planke, S. and Malthe-Sørenssen, A., 2008. Saucer-shaped intrusions: occurrences, emplacement and implications. Earth and Planetary Science Letters, 266(1): 195-204.

45. Pongwapee, S., Won-in, K. and Morley, C.K., 2019. Syn-rift magmatism in a Cenozoic rift basin, from 3D seismic data Wichianburi Sub-basin, Phetchabun Basin, Thailand:

Part 1 distribution and timing of intrusions and forced folds. Journal of the Geological Society: jgs2019-2046.

46. Poppe, S., Holohan, E.P., Galland, O., Buls, N., Van Gompel, G., Keelson, B., Tournigand, P.-Y., Brancart, J., Hollis, D. and Nila, A., 2019. An Inside Perspective on Magma Intrusion: Quantifying 3D Displacement and Strain in Laboratory Experiments by Dynamic X-Ray Computed Tomography. Frontiers in Earth Science, 7: 62.

47. Ramberg, H., 1981. Gravity, deformation and the earth's crust: in theory, experiments and geological application. Academic press, London, 452 pp.

48. Schellart, W., 2000. Shear test results for cohesion and friction coefficients for different granular materials: scaling implications for their usage in analogue modelling. Tectonophysics, 324(1-2): 1-16.

49. Schmiedel, T., Galland, O. and Breitkreuz, C.J., 2017. Dynamics of sill and laccolith emplacement in the brittle crust: Role of host rock strength and deformation mode. Journal of Geophysical Research: Solid Earth, 122(11): 8860-8871.

50. Schmiedel, T., Galland, O., Haug, Ø., Dumazer, G., Breitkreuz, C.J., 2019. Coulomb failure of Earth's brittle crust controls growth, emplacement and shapes of igneous sills, saucer-shaped sills and laccoliths. Earth and Planetary Science Letters, 510: 161-172.

51. Schofield, N.J., Brown, D.J., Magee, C. and Stevenson, C.T., 2012. Sill morphology and comparison of brittle and non-brittle emplacement mechanisms. Journal of the Geological Society, 169(2): 127-141.

52. Spacapan, J.B., Galland, O., Leanza, H.A. and Planke, S., 2017. Igneous sill and finger emplacement mechanism in shale-dominated formations: a field study at Cuesta del

Chihuido, Neuquén Basin, Argentina. Journal of the Geological Society, 174(3): 422-433.

53. Sparks, R., Biggs, J. and Neuberg, J., 2012. Monitoring volcanoes. Science, 335(6074): 1310-1311.

54. Stearns, D.W., 1978. Faulting and forced folding in the Rocky Mountains foreland. Geological Society of America Memoirs, 151: 1-38.

55. Sturkell, E., Einarsson, P., Sigmundsson, F., Geirsson, H., Ólafsson, H., Pedersen, R., de Zeeuw-van Dalfsen, E., Linde, A.T., Sacks, S.I. and Stefánsson, R., 2006. Volcano geodesy and magma dynamics in Iceland. Journal of Volcanology and Geothermal Research, 150(1-3): 14-34.

56. Thomson, K. and Hutton, D., 2004. Geometry and growth of sill complexes: insights using 3D seismic from the North Rockall Trough. Bulletin of Volcanology, 66(4): 364-375.

57. Trude, J., Cartwright, J., Davies, R.J. and Smallwood, J.R., 2003. New technique for dating igneous sills. Geology, 31: 4.

58. van Wyk de Vries, B., Márquez, A., Herrera, R., Bruña, J.G., Llanes, P. and Delcamp, A., 2014. Craters of elevation revisited: forced-folds, bulging and uplift of volcanoes. Bulletin of Volcanology, 76(11): 1-20.

59. Withjack, M.O., Olson, J. and Peterson, E., 1990. Experimental models of extensional forced folds (1). AAPG Bulletin, 74(7): 1038-1054.